Investigating Subcellular Compartment Targeting Effect of Porous Coordination Cages for Enhancing Cancer Nanotherapy

Yu Fang,

Department of Chemistry, Texas A&M University, College Station, TX 77843, USA

Xizhen Lian,

Department of Chemistry, Texas A&M University, College Station, TX 77843, USA

Yanyan Huang,

Beijing National Laboratory for Molecular Sciences, CAS Key Laboratory of Analytical Chemistry for Living Biosystems, Institute of Chemistry, Chinese Academy of Sciences, Beijing 100190, China

Guo Fu,

Department of Biology, Texas A&M University, College Station, TX 77843, USA

Zhifeng Xiao,

Department of Chemistry, Texas A&M University, College Station, TX 77843, USA

Qi Wang,

Department of Chemistry, Texas A&M University, College Station, TX 77843, USA

Beiyan Nan,

Department of Biology, Texas A&M University, College Station, TX 77843, USA

Jean-Philippe Pellois, and

Department of Biochemistry and Biophysics, Texas A&M University, College Station, TX 77843, USA

Hong-Cai Zhou

Department of Chemistry, Texas A&M University, College Station, TX 77843, USA

Abstract

Understanding the key factors for successful subcellular compartment targeting for cargo delivery systems is of great interest in a variety of fields such as bionanotechnology, cell biology, and nanotherapies. However, the fundamental basis for intracellular transportation with these systems has thus far rarely been discussed. As a cargo vector, porous coordination cages (PCCs) have great potential for use in cancer nanotherapy and to elucidate fundamental insight regarding subcellular compartment targeting. Herein, it is shown that the transportation of PCC cargo vectors though various subcellular barriers of the mammalian cell can be manipulated by tuning the vector's electronic property and surface affinity. It is found that the PCCs become selectively aggregated at

Correspondence to: pellois@tamu.edu, zhou@chem.tamu.edu.

the cell membrane, the cytoplasm, or the nucleus, respectively. When a DNA topoisomerase inhibitor is delivered into the nucleus by a neutral and lipophilic PCC, the anticancer efficacy is dramatically improved. The findings shed light to tune the interactions at the "bionano" interface. This study provides a key strategy for future work in targeting specific cell organelles for cell imaging, cargo delivery, and therapy. This research also offers key insight into the engineering of nanoscopic materials for furnishing cell organelle-specificity.

1 Introduction

For a variety of physiologically and therapeutically active agents, targeting and successful uptake into specific subcellular organelles are essential to maximize the efficacy of the agent.[1-4] However, it is a common occurrence that the bioactive compound must be used in considerably high dosages as they often not site specifically on their own. This widespread distribution has been known to cause side effects associated with undesired accumulation of the agents within organelles that are not the desired target.[5] Therefore, cargo transportation vectors and carriers for directed agent delivery have been highly desired. These cargo vectors can be developed to improve the selectivity of organelle targeting, ultimately improving agent activity, while simultaneously reducing harmful overdosage effects for nontargeted organelles.[6-8] In the past few decades, several synthetic nanoscopic delivery platforms, such as cell-permeable peptides (CPPs),[9-14] metal–organic frameworks (MOFs),[15, 16] metal nanoparticles (M NPs),[17] small dendrimers,[18] and carbon nanotubes (CNTs),[19] have been developed as potential intracellular transportation vehicles. However, to the best of our knowledge, very few synthetic materials larger than a few nanometers in diameter can be controllably passed through different biological barriers and reach the desired targeting site.[20] For instance, nano-MOFs have been shown to become trapped within the endosome upon entering the cell, hindering their ability to reach their targets.[16] Most of dendrimers and quantum dots have been proved noncytotoxic, but some of them have been shown to induce a transient partition of the membrane to enter the cell, which is associated with cytotoxicity.[21] Similarly, NPs are generally biocompatible, however, some metal contained NPs have been shown to disrupt the endolysosomal membrane in order to enter the cell, causing immediate cellular damage.[22] These materials have been well investigated for a variety of biological applications. However, for subcellular organelle targeting purposes by using those materials, it requires rational design and laborious synthesis, as well as postfunctionalization. Thus, a novel cargo vector, which is intrinsically nontoxic, easy to synthesize, has a straightforward cargo encapsulation and release mechanism, and can produce controllable intracellular transportation, is urgently needed.

Porous coordination cages (PCCs) are nanoscopic structures assembled by metal clusters and organic linkers, which bears intrinsic porosity in both solid and solution state. The typical particle size of PCC is 1–10 nm, making them potential cellular barrier penetration capability. Stang, Yaghi, Fujita, Raymond, and Nitschke have developed multifunctional tetrahedral, cubic, and octahedral cages containing large pores.[23-27] The PCC structures usually exhibit a hydrophobic inner cavity, water stability, and size uniformity in solution.[28-32] As PCCs can carry guest molecules within these cavities and can release guest molecules as a result of their reversible bonds, PCCs are potential candidates for cellular

cargo delivery vectors. These features are highly desired for photodynamic therapy and chemotherapy applications.[33-36] Their structural diversity and modulated functionality make PCCs potential candidates for enhancing cellular uptake and directing organelle targeting. An additional benefit to using PCCs is that the cytotoxicity of PCC carrier themselves can be minimized by careful selection of biocompatible components.[16, 36-39] Although PCCs have great potential in intracellular delivery, there are currently no reports elucidating their intracellular pathway or for tuning their subcellular compartment-targeting.

We envision that studies regarding controllable subcellular compartment-targeting for a molecular transporter should focus on the size, shape, charge, and affinity of the transporter.[40-42] For the PCC-type molecular transporter, the small size (1–10 nm) makes it a potential candidate for circumventing the endocytosis pathway and pass through various cellular barriers. The charge of the PCCs is usually determined by the surface functional groups, as well as coordination sites in the structure. As both of these aspects of PCCs can be modified, the charge associated with a PCC structure can range from neutral, negative, or positive. With distinctive charge variations, the PCC molecular transporter can exhibit hydro- or lipophilic property. In order to elucidate a transportation mechanism, we sought to design and synthesize PCC molecular transporters with a variety of differentiated charges and affinities, while maintaining an octahedral-shaped structure and approximate size. This was done in order to elucidate the relationship between the subcellular localization of the PCCs and their structural or electronic properties.

2   Results and Discussion

2.1   Synthesis and Characterization of PCCs

Although there are a variety of geometries of PCCs, such as octahedron, tetrahedron, cuboctahedron, and sphere, in this study we want to focus on one topology—octahedron—and only tune the charge and surface affinity. The charge of PCCs is usually dictated by the coordination sites and surface functional groups. First, we selected two PCCs, PCC-1 and PCC-2, with similar carboxylic acid ligand and transition metal cluster (Figure 1a). The difference between them comes from the charge. For PCC-2, anionic sulfate groups (SO3−) replaced tert-butyl groups (tBu) of PCC-1, making the whole structure negatively charged. Then, we introduced PCC-3, a cage with pyridine ligand and noble metal knot (Figure 1a). This cage showed distinct positive net charge and hydrophilic surface. Thus, PCC-1, 2, and 3 covered a broad range of PCC in different property and acted as the prototype for cargo vehicles in coordination cage species.

PCC-1, PCC-2, and PCC-3 were synthesized by the solvothermal method (Section S2, Supporting Information). PCC-1 was readily formed by the reaction of the vertex ligand (H4V1) and panel ligand (H3L1) with ZnCl2 at 120 °C in N,N-dimethylformamide (DMF) for 72 h. The bright yellow polyhedron-shaped crystals of the cage complex PCC-1 were collected upon the completion of the synthesis reaction. Upon analysis by single-crystal X-ray diffraction (SC-XRD), it was determined that PCC-1 crystallizes in the central-symmetric tetragonal space group I4/m. Similarly, PCC-2 was prepared by reacting vertex ligand (Na4H4V2) and panel ligand (H3L2) with CoCl2 at 80 °C in methanol with two drops of Et3N for 24 h, followed the previously reported method.[43] PCC-2 adopts a similar

octahedral hollow cage structure but in the trigonal R3—R3$^-$ space group according to SC-XRD. The last cage in the study, PCC-3, was formed by the reaction of the vertex metal complex [Pd(V3)(NO3)2] and the panel ligand (L3) at 100 °C in H2O for 2 h, according to a previously published procedure.[44]PCC-3 adopts a similar octahedral hollow cage structure to that of PCC-1 and PCC-2, but it crystallizes into a tetragonal P43212 space group. Both of the PCC-1 and PCC-2 cage molecules consist of six tetranuclear metal clusters as vertices (Zn4V1 and Co4V2, respectively) and eight panel ligands as faces (L1 and L2, respectively) assembled into an octahedron cage. Each Zn/Co atom in the cluster is located at the four corners of the cluster square plane and held in a pseudo-octahedral configuration by coordination with six oxygen atoms. The six oxygen atoms include one sulfonic oxygen and two phenolate oxygen atoms from V1 (or V2), two carboxylate oxygens from two adjacent L1 (or L2), and a μ4-OH2 (or μ4-OH). The assignment of the central oxygen atom as a μ4-OH2 or a μ4-OH depends on the synthetic condition.[45, 46] Unlike PCC-1 or PCC-2, PCC-3 consists of six mononuclear metal clusters {[Pd(V3)]2+} located at the vertices and four panel ligands which become the faces of the cage. Six vertices and four panel ligands are assembled into an octahedron cage, leaving the other four faces of the cage open. In the structure of PCC-3, each Pd atom is held in a square planar configuration through coordination to two nitrogen atoms from one V3 and two nitrogen atoms from two individual L3. Based on the crystal structures of the three PCCs, the longest inner-cavity distances are 31.3, 25.1, and 12.7 Å for PCC-1, PCC-2, and PCC-3, respectively. The largest outer diameters for the cages are 50.0, 42.2, and 28.0 Å for PCC-1, PCC-2, and PCC-3, respectively. From the packing diagram of the three cages, we were able to determine the presence of microporosity and mesoporosity in the solid state, indicating that PCCs are porous materials (Figures S13, S16, and S18, Supporting Information). Nitrogen gas adsorption study shows the intrinsic porosity of PCC-1 (Figure S19, Supporting Information).

Although the three cages share a similar octahedral structure, their individual net charges and affinity are totally different. For PCC-1, the 48 positive charges from the Zn2+ metal ions in the clusters are fully compensated by the phenolate groups from the combined V1 ligands (24 negative charges) and the carboxylate groups from the panel ligand L1 (24 negative charges). Thus, PCC-1 possesses a zero-net charge and gives a neutral host, {[Zn4(μ4-OH2)V1]6(L1)8}0. For PCC-2, the negative charge is derived from a combination of sulfate groups from the V2 ligand (24 additional negative charges) and the hydroxyl groups (6 negative charges) in the Co clusters. Thus, PCC-2 gives an anionic host as {[Co4(μ4-OH)V2]6(L2)8}30− with Na+ and Et3NH+ as counter cations. For PCC-3, since the pyridyl ligands (V3 or L3) do not bear charge, the positive charge in the structure originates with the six Pd2+metal centers. Thus, PCC-3 gives a cationic host as {[PdV3]6(L3)4}12+, with NO3− as the counter anions. In addition, PCC-1 and PCC-2 are soluble in the polar solvents, such as dimethyl sulfoxide (DMSO) and miscible with H2O. However, PCC-3 readily dissolves in H2O, whereas hardly dissolved in organic solvents. As a result of the solubility of the individual cage species, PCC-1 and PCC-2 were deemed lipophilic and PCC-3 was deemed hydrophilic. The differences in the charge and the affinity of the cage may affect the cellular uptake of the cages.

Nuclear magnetic resonance (NMR) spectroscopy was used to identify the formation of PCC-1 and PCC-3 as single independent species in high purity (Figures S8 and S11, Supporting Information). Matrix-assisted laser desorption/ionization-time-of-flight-mass spectroscopy (MALDI-TOF-MS) was used to confirm that PCC-1 has a neutral charge and was identified by a single molecular peak at the appropriate m/z (Figure S9, Supporting Information). Electrospray ionization-mass spectroscopy (ESI-MS) unambiguously showed the ionic fragment distribution of both the negatively charged PCC-2 (Figure S10, Table S1, Supporting Information). Thermogravimetric analysis (TGA) was used to indicate that all three of the PCCs are thermally stable up to 440 °C (Figures S20-Supporting Information). Furthermore, UV-vis spectroscopy (Figure S23, Supporting Information) was also applied to characterize the formation of PCC-1. Of significant importance for cellular transportation distribution studies, the fluorescence property of panel ligand (L) was maintained in the PCC-1 structure post synthesis (Figure S24, Supporting Information). The fluorescent properties of PCC-1 are of significance as to date, there are very few reported metal-organic cages that maintain intrinsic fluorescence.[47-49] Of the three PCCs, PCC-1 is the only one in this study that has intrinsic fluorescence. However, because PCC-2 and PCC-3 both possess internal cavities, both cages can become fluorescent by encapsulating fluorescent dye. Thus, studies of cellular distribution and transportation for PCC-2 and PCC-3 could be accomplished without the cages possessing intrinsic fluorescence or altering the cage.

2.2 Cargo Encapsulation and Release of PCCs

Investigations into the guest molecule encapsulation and release properties of the PCCs (Figure 2a) were also conducted in vitro. Since all three of the cages have hydrophobic internal cavities, it is proposed that they encapsulate guest molecules through hydrophobic interactions. In addition to hydrophobic interactions, electronic interactions for encapsulation could be engineered for PCC-2 and PCC-3 because these cages have net charges. This property may be useful as it can be used in order to maintain strong interactions between host and guest during intracellular transportation. (+)-Camptothecin (CPT), Rhodamine B (RB), and Nile Red (NR) were selected to be the guest molecules for the PCC cages (Figure 2g, and Figure S23, Supporting Information). Because PCC-1 is intrinsic fluorescent, choosing an anticancer drug (CPT) as the guest of PCC-1 can further investigate its anticancer efficacy. Neither PCC-2 nor PCC-3 is fluorescent. Thus, a cationic fluorescent dye (RB) was assigned to be the guest of PCC-2, while a hydrophobic dye (NR) was assigned to be the guest of PCC-3. The proposed cargo@PCC complexes are shown in Figure 2b-d and were generated using molecular modeling. To achieve successful loading, 50 mg of the activated single crystal of PCC-1 was soaked in a solution of 6 mg CPT in 10 mL ethanol and stirred at room temperature for 24 h. Then the supernatant was separated by centrifugation and analyzed by UV–vis spectrum. By comparing the initial and final concentration, we were able to confirm the formation of cargo@PCC complex CPT@PCC-1 and gain nearly four molecules (loading wt = 0.110 g g−1, 93% loaded) (Figure 2b, and Figures S26 and S27, Supporting Information). NR was also encapsulated by PCC-1 to give complex NR@PCC-1. A similar loading procedure for RB was done for PCC-2 (loading wt = 0.076 g g−1, 94% loaded) (Figure 2c, and Figures S28 and S29, Supporting Information). For PCC-3, the dye encapsulation procedure was conducted in water media. When solid NR (8.9 mg; insoluble in water) was suspended in a H2O solution of PCC-3 (50 mg, 10 mL) at

80 °C for 1 h, the host–guest complex was formed quantitatively which was characterized by 1H NMR (loading wt = 0.178 g g−1, 100% loaded) (Figures S32 and S33, Supporting Information). Besides, UV–vis and fluorescence spectroscopy was used to identify the successful formation of the cargo@PCC complexes (Figure 2e, and Figures S30 and S34, Supporting Information). All the UV–vis studies were carried out at 25 °C and the same concentration (2.5 µg mL−1). The DMF solution containing 2.5 µg mL−1 of CPT@PCC-1 and RB@PCC-2 showed maximum absorption wavelength at 350 and 550 nm, respectively. The aqueous solution of NR@PCC-3 (2.5 µg mL−1) showed maximum absorption wavelength at 581 nm. Comparing to the excitation spectra of free cargos, the cargo-PCC complexes showed obvious redshifting (2–46 nm), indicating the successful cargo encapsulation. From the emissionspectra of cargo-PCC complexes (Figure 2f, and Figures S31 and S35, Supporting Information), the emission wavelength is 497, 592, and 606 nm for CPT@PCC-1, RB@PCC-2, and NR@PCC-3, respectively. The distinct fluorescent property of the cargo@PCC complexes will allow further investigation for monitoring their cellular transportation.

Previously, one of the major hinderance by using coordination cages in cellular environment is their low stability under physiological condition (pH = 7.4–6.5) in the presence of anions and proteins. The drug release of cargo@PCCs was also studied in PBS solutions at a variety of pH values. After extracting the released cargo from PBS solution after a different period of time and measured by UV–vis (Figure 2h) and 1H NMR, the cargo release increased upon the elongating of time. In the neural environment (pH = 7.4, mimicking nucleus and cytosol environment), drug release of CPT@PCC-1 was initiated from 16 h, and reached 100% release after 7 d. When the pH of the buffer solution was lowered to pH = 6.5 (mimicking endosome and lysosome environment), the release of CPT from PCC-1 started earlier (4 h) and was completed within a shorter time (96 h). For RB@PCC-2, the cargo release was initiated from 4 h, and completed release after 120 h. Under pH = 6.5, the release of PCC-2 started from 2 h and completed within 72 h. In contrast, the stability of PCC-3 under the neutral condition is relatively high. NR started to be released from PCC-3 from 72 h and after 7 d the release ratio reached 15%. When increasing the acidity of PBS buffer (pH = 6.5), the NR release of NR@PCC-3 complexes started at 8 h, and the release ratio is 56% after 7 d. Overall, these data indicate that PCCs may remain stable and retain its drug payload for several hours while being transported outside and inside cells. Since the cytoplasm and nuclear are essentially neutral, capsule disassembly and subsequent drug release may then occur at a constant rate. The pH-responsive cargo release feature of PCC carriers make them more suitable for tumor tissue drug delivery.[50]

2.3 Intracellular Transportation of PCCs Monitored by Confocal Laser Scanning Microscopy (CLSM) and Epifluorescence Microscopy (EFM)

A study of the cellular internalization of CPT@PCC-1, RB@PCC-2, and NR@PCC-3 was accomplished by the incubation of the complexes with live HeLa cells in culture media with a concentration of 2.5 µg mL−1 for 2 h. The cellular distribution of each of the cargo-PCC complexes was studied using CLSM (Figure 3a). For a control comparison, we also performed the cellular uptake experiments with free CPT, RB, and NR using the same experimental uptake procedure. The results are summarized in Table 1.

According to our control experiments as well as previously reported literature results, most of the free CPT were distributed in the cytoplasm.[51-55] As expected, images taken using CLSM indicated CPT predominantly located in the cytoplasm as seen by a very weak fluorescence (405 nm excitation) of the drug in this part of the cell. In stark contrast to the results of the control, CPT@PCC-1 accumulated preferentially in the nucleus rather than in the cytoplasm. This was determined by a very bright fluorescence signal in the nucleus of the cell by CLSM (405 nm excitation). As CPT needs to maintain nuclear accumulation to show anticancer activity since this drug is designed to be most effective in the nucleus, the nuclear accumulation of CPT@PCC-1 is extremely desirable.[52] Since CPT drug and PCC-1 have similar fluorescence color, we further explored the co-incubation of PCC-1 and red color NR, as well as the incubation of NR@PCC-1. Figure 3b clearly shows that PCC-1 accumulated both in nuclear and cytoplasm (blue color), while NR only distributed in the cytoplasm (red color). As our expectation, the overlapped zone (purple color) is mainly in the cytoplasm. On the contrary, for NR@PCC-1, co-localization visualized by purple signals was found exclusively occupied in the nucleus, strongly indicating the cargo carriers were intact when they were introduced into cellular environments (Figure 3b). To elucidate the cellular internalization and nuclear entering mechanism of CPT@PCC-1, it was incubated with HeLa cells in the presence of amiloride, a macropinocytosis inhibitor, or at 4 °C, a condition that inhibits energy-dependent transport pathways.[56,57] In both cases, CPT@PCC-1 was still capable of entering the cells (Figure S37, Supporting Information). These data, therefore, indicate that internalization of CPT@PCC-1 happened most likely through translocation instead of endocytosis. In addition, at 4 °C, the accumulation of CPT@PCC-1 in the nucleus was dramatically reduced, which indicates that the transportation of CPT@PCC-1 into the nucleus is energy-dependent (Figure S37, Supporting Information). We also found that intranuclear accumulation of CPT@PCC-1 is possible for Skov 3, H1299, and HepG2 cells, which indicates that nuclear transportation of PCC-1 is not cell-specific (Figure S38, Supporting Information).

From the CLSM images, free RB mainly bind to the mitochondria by showing bright reticulum fluorescent signals. These results are well known as mitochondria bear a negative charge and cationic RB has been used as mitochondria dye in the literature.[53] In contrast to free RB, the highly negative complex RB@PCC-2 exhibited evenly distributed in the cytoplasm and had no visible mitochondrial binding. We presume this phenomenon to be the highly negative property of RB@PCC-2 inducing charge repulsion between itself and the mitochondria. As a neutral and lipophilic dye, free NR mainly binds to the lipid droplets within a cell. This can be seen using CLSM as NR appears by showing spherical bridge fluorescent spots.[54] Differing from free NR, NR@PCC-3 was shown to not enter the cell at all and was rather predominantly located on the cytoplasm membrane. We ascribe this phenomenon to the intrinsic positive charge of the PCC-3 cage causing the complex to be strongly attracted to the negatively charged cell membrane surface.[55] The results of the in vitro studies indicate that PCC-1, PCC-2, and PCC-3 show completely different subcellular distributions from one another owing to their distinctive charge features. In addition, PCC cargo capsules altered the subcellular distribution of the encapsulated cargos, which has potential as subcellular compartment-targeting vectors (Table 1). It is worth mentioning that each of the PCCs in this study adopted totally different cellular distributions to traditional

NPs. For example, it is known that cationic Au NPs pass through the cell membrane by direct diffusion, whereas anionic Au NPs enter a cell through endocytosis.[58, 59] In contrast, cationic PCC-3 adheres on the cell membrane, and anionic PCC-2 enters the cell by translocation. The distinct subcellular distribution of PCCs should be ascribed to their charge and affinity difference. Since PCC-1 is neutral and hydrophobic, it can pass through the cytoplasm and entered the nucleus. As an anionic cage, PCC-2 is also capable of entering the cytoplasm, however charge repulsion prohibits it from entering the nucleus, because nucleus is also negatively charged. The anionic nature of PCC-2 allows it (and the cargo it carried) to evenly distribute in the cytoplasm. In the contrary, because of the cationic surface, PCC-3 can only be attracted to the outer cytoplasm of a cell. Once the cytoplasm has been removed (in a permeabilized cell), PCC-3 can enter the cytosol, however, the hydrophilic nature stops it from entering the nucleus. Of significant importance is that the PCCs in this study demonstrate the capability of manipulating the subcellular distribution of the guest molecules they carry. On a fundamental basis, this provides important knowledge for PCCs as potential tools for vector-mediated delivery for cell organelle targeting. Since the cytoplasm membrane is the first and sometimes the dominant cellular barrier toward nanoparticle, we tend to remove the cytoplasm membrane to see whether the subcellular distribution of PCCs can be altered. According to literature reported method,[60, 61] we treated the HeLa cells with Digitonin[62] to obtain permeabilized cells. The processes by which the binding of the complexes to the cell organelles were monitored by EFM (Figure 3c). For CPT@PCC-1, the clear transportation from the cytosol to the nucleus was recorded (see Video S1, Supporting Information). After the cytoplasm membrane was compromised, PCC-1 entered the nucleus within 30 s, which is considerably faster than that of intact cell (30 min). Since the cytosol and nuclear transportation protein (NTP) were removed from permeabilized cells, PCC-1 was still capable of accumulating within the cell nucleus, suggesting the nuclear transportation of it is cytosol and NTP independent. Again, no nuclear transportation was observed for RB@PCC-2 or NR@PCC-3 under the same conditions (Figure 3c, and Videos S2 and S3, Supporting Information). For RB alone, it showed relatively weak signals in the cytosol. However, it seems that RB@PCC-2 was not affected by the change of cellular environment, by showing strong signals in the cytosol. The anionic nature of PCC-2 allows the even distribution of encapsulated RB in the cytosol of permeabilized cells. Interestingly, after the cytoplasm membrane was compromised, NR@PCC-3 is now capable of entering the cell, by localizing in cytosol and mitochondria. Because PCC-3 is cationic, the binding to mitochondria ascribed to the electrostatic attractions. However, PCC-3 hardly enter the nucleus, probably because the hydrophilic surface of PCC-3 hardly pass through the hydrophobic channel of NPCs.[63-65] In summary, we again observe the PCC cargo vectors are capable of tuning the cellular distribution of encapsulated cargos in the permeabilized cells. According to the phenomenon we observed, it suggested that the electronic property of cargo vectors determines the cellular entrance step, while the surface affinity of them determines the nuclear-entering step.

2.4 Anticancer Efficacy Investigated by CPT@PCC Complexes

Finally, we explored cytotoxicity of these PCC cages and whether the anticancer efficacy can be affected by the targeted delivery to designated subcellular compartments. First, the CPT were encapsulated by PCC-1, PCC-2, and PCC-3 according to the procedure in Section

2.2. Second, the cytotoxicity of empty PCCs, free CPT, and CPT@PCCs toward HeLa cell was measured with Sytox Green assay and yellow 3-(4,5-dimethythiazol-2-yl)-2,5-diphenyl tetrazolium bromide (MTT) assay. After treatment of the solutions of PCCs at 2.5, 5.0, and 10.0 or 15.0 μg mL−1 concentration, the remaining number and morphology of the cell can be calculated and distinguished through CLSM. As shown in the bright-field images of Figure 4a, when treated with empty PCCs, the number of the cell remained high, and the remaining cells remained healthy. According to the assay, the survival rates of different empty PCC samples are above 80% (Figure 4b). This is consistent with the previous findings that Zn ions, carboxylic acid ligands, pyridyl ligands, and calix[4]arenes are typically not toxic.16, 36-39 In contrast, the CPT group showed apoptotic morphology such as round-up (Figure 4c), shrinking and detached, giving a 52% survival rates of the cell (Figure 4d). Besides, the viability of HeLa cells treated with free CPT showed a concentration-dependent fashion (Figure 4d). The relative moderate anticancer efficacy of CPT is likely due to the poor cell penetrability and nuclear accumulation of CPT on its own. Notably, when treated with CPT@PCC-1, the amounts of cells are dramatically reduced compared with other groups. And there is a large portion of remaining cells dead (green fluorescent dots), according to Sytox Green assay (Figure 4c). As a result, the viability of the CPT@PCC-1 groups dropped to 9.5% for HeLa cells (Figure 4d). Student's t-test results show an extreme significant difference ($P < 0.05$) between CPT@PCC-1 group and free CPT group. MTT assay gave exactly the same results (Figure S39, Table S4, Supporting Information). The anticancer efficacy studies of free CPT and CPT@PCC-1 revealed the effectiveness of PCC-1 for the nucleic delivery of CPT. On the other hand, CPT@PCC-2 and CPT@PCC-3 groups remain above 60% cell viability, indicating CPT drug was not taking effect at the cytosol or cytoplasm membrane site (Figure 4d). The cytotoxicity of CPT@PCC-2 and CPT@PCC-3 is even lower than the CPT drug alone at the same concentration. The clear differences in cytotoxicity for CPT and CPT@PCCs further support the correlation between the delivery position and the anticancer efficacy of the drug. From cell viability experiments, we realize that the totally different cell compartment targeting effect of PCCs will considerably affect the cytotoxicity of the cargo carrier, thus giving different anticancer efficacy. By bringing specific cargos to their targeting site via PCCs, we can expect the anticancer efficacy of the cargos will be boosted.

3   Conclusions

In summary, we applied three porous coordination cages as cargo vectors for cellular uptake and investigated their cell compartment targeting, as well as anticancer efficacy. Although the three cages share a similar structure, they show different subcellular distributions as a result of their varied charge and affinity features. The results of this study were able to determine that the properties of charge and affinity are the dominant factors for tuning cell compartment targeting for PCC-based cargo vectors within living mammalian cells. We also proved that, when a specific bioactive agent was brought to its targeting site by PCC, the anticancer efficacy was dramatically improved. Furthermore, PCCs exhibit a different cellular uptake pathway and distribution when compared to well-studied Au NPs. The unique behavior of PCC-1, PCC-2, and PCC-3 suggests that PCCs could be a powerful tool for the manipulation of the cellular transportation pathway and the delivery target position of

their respective guest molecules. With a vast array of possible structural modifications available for PCCs, further investigations regarding the property-interaction relationships of these cages in terms of "bionano" interface engineering will be demonstrated in the near future.

4   Experimental Section

Synthesis of H3L1:

H3L1 was synthesized by four steps of organic synthesis from commercial starting material phenothiazine. The detailed synthesis route and full characterizations are provided in the Supporting Information.

Synthesis of PCC-1:

H3L1 (21 mg, 0.033 mmol), H4V1 (12 mg, 0.014 mmol), and ZnCl2 (14 mg, 0.103 mmol) were dissolved in 1 mL DMF. The mixture was heated to 120 °C in an oven for 48 h. After cooling to ambient temperature, the bright yellow crystals were collected and washed with methanol. Yield of PCC-1 (based on H3L1): ≈80% (according to ligand H3L). 1H NMR (300 MHz, d7-DMF) δ 8.21 (br, 32H, L), 8.04 (br, 48H, L), 7.99 (br, 48H, V),7.80 (br, 32H, L), 7.67 (br, 16H, L), 7.58 (br, 16H, L), 7.45 (br, 16H, L), 6.43 (br, 16H, L), 1.20 (s, 216H, V). 13C NMR (75 MHz, d7-DMF) δ 167.52, 167.48, 143.56, 143.35, 143.08, 140.37, 139.74, 133.91, 131.47, 130.50, 130.34, 129.68, 128.42, 128.11, 127.51, 126.38, 125.56, 125.27, 120.12, 116.82, IR, 2963, 2926, 2854, 1720, 1606, 1436, 1278, 1180, 1112, 1016, 780, 736, 604, 563, 497,480. MS, elemental analysis: calculated (%) for [C552H452N8O126S32Zn24]·8DMF·30H2O, C 53.49, H 4.43, N 1.73, S 7.93; found (%): C 53.88, H 4.13, N 1.25, S 8.17. MALDI-TOF-MS: theoretical: 11 764.30; found: 11 764.41.

X-Ray Single-Crystal Structure Analyses:

All crystals were taken from the mother liquid without further treatment, transferred to oil and mounted into a loop for single-crystal X-ray data collection. Diffraction was measured on a Bruker Smart Apex diffractometer equipped with a MoKα sealed-tube X-ray source (λ = 0.71073 Å, graphite monochromated) and a low-temperature device (110 K). The data frames were recorded using the program APEX2 and processed using the program SAINT routine within APEX2. The data were corrected for absorption and beam corrections based on the multiscan technique as implemented in SADABS. The structures were solved by direct method using SHELXS and refined by full-matrix least-squares on F2 using SHELXL software.

Cargo Encapsulation:

Procedure 1: 50 mg of activated single crystal of PCCs was soaked in a solution of 6 mg of cargo in 10 mL ethanol, and stirred at room temperature for 24 h. Then the supernatant was separated by centrifugation and analyzed by UV–vis spectrum. The initial and final concentration of the cargo solution was measured to calculate the encapsulated drug amount. After drug encapsulation, the drug included crystal cargo@PCCs was washed by ethanol for three times and dried in air. Then the after washes crystal of cargo@PCCs was also put into

ethanol solution for another 24 h to check the guest leaching. This procedure was applied to the synthesis of CPT@PCC-1, CPT@PCC-2, NR@PCC-1, and RB@PCC-2.

Procedure 2: When a solid cargo (8.9 mg) was suspended in a H2O solution (50 mg, 10 mL) of PCC and the resulting solution was stirred at 80 °C for 1 h, the solution color turned from pale yellow to blue. After removal of residual cargo by filtration, 1H NMR confirmed the formation of dye-cage complex cargo@PCC. From the NMR integration, the amount of encapsulated cargo molecules was calculated. This procedure was applied to the synthesis of NR@PCC-3 and CPT@PCC-3.

Cargo Release:

Suspending 10 mg of Cargo@PCC-1 material in 20.0 mL of buffer solution (pH 7.4 and 6.5, respectively) at 37 °C. The release system was then maintained at 37 °C under shaking (shaking frequency = 150 rpm). 1 mL of release medium was sampled at each time point, and UV–vis spectrophotometry was used to determine the percentage of cargo that was released, after which the sample was returned to the original release system. The amount of cargo released was determined from the UV–vis absorbance at specific wavelength. The release percentages of cargo were calculated according to the formula, release percentage (%) = (released cargo)/(loaded cargo).

Cell Uptake Pathway and Cellular Transportation Monitored by CLSM: Cells were seeded and grown to 80–90% confluency in 1–2 d on a 48-well plate. The cells were incubated with free CPT, PCC-1, CPT@PCC-1, NR@PCC-1, RB@PCC-2, and NR@PCC-3 (2.5 μg mL-1 Leibovitz's L-15 media that did not contain cysteine, nrL-15) for a variable period of time. Cells were washed with nrL-15 twice. Images were collected using a Rolera-MGI Plus back-illuminated electron-multiplying charge-coupled device (EMCCD) and camera (Qimaging). Images were acquired using bright-field imaging and a standard fluorescence filter sets: CFP (excitation (Ex) = 436 ± 10 nm/emission (Em) = 480 ± 20 nm). The fluorescence intensities of the different cells were measured with the SlideBook 4.2 software (Olympus), and the average fluorescence intensity was determined for each condition. Intracellular transportation of CPT@PCC-1 and organic ligand H3L1 was monitored for 30 min. Intranuclear delivery of CPT@PCC-1 was observed for HeLa, Skov 3, H1299, and HepG2 cells. As a control experiment, endocytosis inhibitor (amiloride) was added to the CPT@PCC-1 group, and then the cellular transportation behaviors were observed.

Nuclear Transportation Monitored by EFM:

For microscopy, flow cells were transferred to an eight-well glass plate. Cells were washed with Leibovitz's L-15 media that did not contain cysteine, nrL-15, permeabilized for 2 min with 40 μg mL−1 digitonin in the buffer, and washed again with the buffer twice. A cover slip was added immediately on the top of the pad, and the obtained slide was analyzed by microscopy using a Delta-Vision microscope. Typical time-lapse movies were shot for 5 min with frames captured every 2 s. For fluorescence microscopy, the images were captured with the FITC filter or Rhodamine filter. To avoid blue light toxicity, the time of illumination was limited to 0.5 s in the presence of a 50% neutral density filter. The fluorescent intensity of nuclear and cytoplasm was measured and recorded by EFM, followed by making figures by

using Image J software. Movies were obtained by processing the series of images collected with the Quick Pro Time software (see Videos S1-S3, Supporting Information).

Cytotoxicity Assays (Sytox Green):

The cells were seeded in 96-well plates at a density of about 2000 cells mL^{-1} and cultured for 24 h. Free drug CPT, empty PCCs, and CPT@PCCs (2.5, 5.0, 10.0, and 15.0 µg mL^{-1} DMEM solution) were incubated with cells for 24 h. Then the media was removed and cells were washed with PBS for twice. Then, the cells were soaked in nrL-15 and treated with dyes. Cell nuclei were stained with Hoechst 33342 for 15 min and dead cell nuclei were stained with SYTOX Green for 15 min. Images were collected using a Rolera-MGI Plus back-illuminated EMCCD camera (Qimaging). Images were acquired using bright-field imaging and two standard fluorescence filter sets: DAPI (excitation (Ex) = 360 ± 10 nm/emission (Em) = 460 ± 20 nm); FITC (Ex = 488 ± 10 nm/Em = 520 ± 20 nm). Blue and green images were collected with all samples. ImageJ was used to count the number of blue and green cells. Multiple times of tests were done to test repeatability. Data and error bars of statistical analysis for uptake and cytotoxicity studies represent the mean ± SEM of at least five independent experiments. Statistical analyses for comparison of free drug (CPT), PCC-1, and CPT@PCCs were carried out using Student's t-test. Results with $P < 0.05$ were considered significantly different and $P < 0.01$ were considered extreme significantly different. Curve fitting of the cytotoxicity data was performed using Graph Pad Prism 6.0. Best nonlinear regression curve fittings were chosen by evaluating R^2, sum of square, and the standard deviation of residuals.

Cytotoxicity Assays (MTT):

The cells were seeded in 96-well plates at a density of about 2000 cells mL^{-1} and cultured for 24 h. Free drug CPT, empty PCCs, and CPT@PCCs (2.5, 5.0, 10.0, and 15.0 µg mL^{-1} DMEM solution) were prepared in cultured medium and added to the wells. After incubation for another 24 h at 37 °C with 5% CO_2, cell viability was determined by MTT assay. The culture medium was carefully removed, and 100 µL of freshly prepared MTT solution (2.5, 5.0, 10.0, and 15.0 µg mL^{-1} in culture medium) was added to each well. After incubation at 37 °C for 4 h, the MTT solution was removed, and 100 µL of DMSO was added to dissolve the formazan crystals. The plate was shaken for 10 min to fully dissolve formazan and homogenize. Absorbance values of the wells were read with a microplate reader at 492 nm (BIO RAD, iMark). The cell viability rate (VR) was calculated from the following equation: VR = A/A0 × 100%, where A is the absorbance of the experimental group and A0 is the absorbance from the cells cultured in serum-supplemented medium without any treatment. All data were obtained from three repeatedly parallel experiments. Statistical analyses for comparison of free drug (CPT), PCC-1, and CPT@PCCs were carried out using Student's t-test. When P-values were 0.05 or less, differences were considered statistically significant. [Crystallographic data for the reported crystal structures have been deposited at the Cambridge Crystallographic Data Centre via www.ccdc.cam.ac.uk with codes 1528505 (PCC-1), 1552521 (PCC-2), and 155770 (PCC-3)].

[The movies for monitoring cell internalization and nucleus transportation were recorded as .avi files. They were attached as Video S1 (Supporting Information)-CPT@PCC-1, Video S2 (Supporting Information)-RB@PCC-2, and Video S3 (Supporting Information)-NR@PCC-3].

Supplementary Material

Refer to Web version on PubMed Central for supplementary material.

Acknowledgements

References:

1. Zheng N, Tsai HN, Zhang X, Rosania GR, Mol. Pharm 2011, 8, 1619. [PubMed: 21805990]

2. Rosania GR, Curr. Top. Med. Chem 2003, 3, 659. [PubMed: 12570858]

3. Feng MR, Curr. Drug Metab 2002, 3, 647. [PubMed: 12369891]

4. Berry JP, Lespinats G, Escaig F, Boumati P, Tlouzeau S, Cavellier JF, Histochemistry 1990,93, 397. [PubMed: 2139017]

5. Li X, Wang L, Fan Y, Feng Q, Cui F-Z, J. Nanomater. 2012, 2012, 548389.

6. Bae YH, Park K, J. Controlled Release 2011, 153, 198.

7. Vasir JK, Labhasetwar V, Technol. Cancer Res. Treat 2005, 4, 363. [PubMed: 16029056]

8. Firer MA, Gellerman G, J. Hematol. Oncol 2012, 5, 70. [PubMed: 23140144]

9. Lindsay MA, Curr. Opin. Pharmacol 2002, 2, 587. [PubMed: 12324264]

10. Bennett RP, Dalby B, Nat. Biotechnol 2002, 20, 20. [PubMed: 11753353]

11. Derossi D, Joliot AH, Chassaing G, Prochiantz A, J. Biol. Chem 1994, 269, 10444. [PubMed: 8144628]

12. Rothbard JB, Jessop TC, Wender PA, Adv. Drug Delivery Rev 2005, 57, 495.

13. Vives E, Brodin P, Lebleu B, J. Biol. Chem 1997, 272, 16010. [PubMed: 9188504]

14. coupade C, Fittipaldi A, Chagnas V, Michel M, Carlier S, Tasciott E, Darmon A, Ravel D,Kearsey J, Giacca M, Cailler F, Biochem. J 2005, 390, 407. [PubMed: 15859953]

15. Horcajada P, Gref R, Baati T, Allan PK, Maurin G, Couvreur P, Férey G, Morris RE,Serre C, Chem. Rev 2012, 112, 1232. [PubMed: 22168547]

16. Zheng H, Zhang Y, Liu L, Wan W, Guo P, Nyström AM, Zou X, J. Am. Chem. Soc 2016,138, 962. [PubMed: 26710234]

17. Yu J, Patel SA, Dickson RM, Angew. Chem., Int. Ed 2007, 46, 2028.

18. Leroueil PR, Hong SY, Mecke A, Baker JR, Orr BG, Holl MMB, Acc. Chem. Res 2007,40, 335. [PubMed: 17474708]

19. Kostarelos K, Lacerda L, Pastorin G, Wu W, Wieckowski S, Luangsivilay J, Godefroy S,Pantarotto D, Briand J-P, Muller S, Prato M, Bianco A, Nat. Nanotechnol 2007, 2, 108. [PubMed: 18654229]

20. Verma A, Uzun O, Hu Y, Hu Y, Han H-S, Watson N, Chen S, Irvine DJ, Stellacci F, Nat. Mater 2008, 7, 588. [PubMed: 18500347]

21. Lovric J, Bazzi HS, Cuie Y, Fortin GR, Winnik FM, Maysinger D, J. Mol. Med 2005, 83,377. [PubMed: 15688234]

22. Hu Y, Litwin T, Nagaraja AR, Kwong B, Katz J, Watson N, Irvine DJ, Nano Lett 2007, 7,3056. [PubMed: 17887715]

23. Olenyuk B, Whiteford JA, Fechtenkotter A, Stang PJ, Nature 1999, 398, 796. [PubMed: 10235260]

24. Sudik AC, Millward AR, Ockwig NW, Côte AP, Kim J, Yaghi OM, J. Am. Chem. Soc2005, 127, 7110. [PubMed: 15884953]

25. Sato S, Lida J, Suzuki K, Kawano M, Ozeki T, Fujita M, Science 2006, 313, 1273. [PubMed: 16946067]

26. Kaphan DM, Levin MD, Bergman RG, Raymond KN, Toste FD, Science 2015, 350,1235. [PubMed: 26785485]

27. Mal P, Breiner B, Rissanen K, Nitschke JR, Science 2009, 324, 1697. [PubMed: 19556504]

28. Dai F-R, Sambasivam U, Hammerstrom AJ, Wang Z, J. Am. Chem. Soc 2014, 136, 7480. [PubMed: 24787363]

29. Fang Y, Murase T, Sato S, Fujita M, J. Am. Chem. Soc 2013, 135, 613. [PubMed: 23270387]

30. Bilbeisi RA, Clegg JK, Elgrishi N, Hatten XD, Devillard M, Breiner B, Mal P, Nischke JR, J. Am. Chem. Soc 2012, 134, 5110. [PubMed: 22043943]

31. Mugridge JS, Bergman RG, Raymond KN, J. Am. Chem. Soc 2010, 132, 16256. [PubMed: 20977233]

32. Liu M, Liao W, Hu C, Du S, Zhang H, Angew. Chem., Int. Ed 2012, 51, 1585.

33. Therrien B, Top. Curr. Chem 2012, 319, 35. [PubMed: 21952848]

34. Zheng Y, Suntharalingam K, Johnstone TC, Lippard SJ, Chem. Sci 2015, 6, 1189. [PubMed: 25621144]

35. Schmitt F, J. Am. Chem. Soc 2012, 134, 754. [PubMed: 22185627]

36. Samanta SK, Moncelet D, Briken V, Isaacs L, J. Am. Chem. Soc 2016, 138, 14488. [PubMed: 27723965]

37. Sun C-Y, Qin C, Wang X-L, Su Z-M, Expert Opin. Drug Delivery 2013, 10, 89.

38. Tamames-Tabar C, Cunha D, Imbuluzqueta E, Ragon F, Serre C, Blanco-Prieto MJ,Horcajada P, J. Mater. Chem. B 2014, 2, 262.

39. Hu Q, Yu J, Liu M, Dou Z, Yang Y, J. Med. Chem 2014, 57, 5679. [PubMed: 24922463]

40. Colvin V, Environ. Mol. Mutagen 2007, 48, 533.

41. Jackson AM, Myerson JW, Stellacci F, Nat. Mater 2004, 3, 330. [PubMed: 15098025]

42. DeVries GA, Brunnbauer M, Hu Y, Jackson AM, Long B, Neltner BT, Uzun O,Wunsch BH, Stellacci F, Science 2007, 315, 358. [PubMed: 17234943]

43. Fang Y, Li J, Togo T, Jin F, Xiao Z, Liu L, Drake H, Lian X, Zhou H-C, Chem 2018, 4, 555.

44. Kusukawa T, Yoshizawa M, Fujita M, Angew. Chem., Int. Ed 2001, 40, 1879.

45. Dai F, Wang Z, J. Am. Chem. Soc 2012, 134, 8002. [PubMed: 22551401]

46. Du S, Hu C, Xiao J, Tana H, Liao W, Chem. Commun 2012, 48, 9177.

47. Yan L, Tan C, Zhang G, Zhou L, Bunzli J, Sun Q, J. Am. Chem. Soc 2015, 137, 8550. [PubMed: 26065490]

48. Neelakandan PP, Jimenez A, Thoburn JD, Nitschke JR, Angew. Chem 2015, 127, 14586.

49. Yan X, Cook TR, Wang P, Huang F, Stang PJ, Nat. Chem 2015, 7, 342. [PubMed: 25803473]

50. Kato Y, Ozawa S, Miyamoto C, Maehata Y, Suzuki A, Maeda T, Baba Y, Cancer Cell Int.2013, 13, 89. [PubMed: 24004445]

51. Barua S, Mitragotri S, ACS Nano 2013, 7, 9558. [PubMed: 24053162]

52. Hsiang Y, Hertzberg R, Hecht S, Liu LF, J. Biol Chem 1985, 260, 14873. [PubMed: 2997227]

53. Johnson LV, Walsh ML, Chen LB, Proc. Natl. Acad. Sci. USA 1980, 77, 990. [PubMed: 6965798]

54. Greenspan P, Mayer EP, Fowler SD, J. Cell Biol 1985, 100, 965. [PubMed: 3972906]

55. Gurnev A, Yang S-T, Melikov KC, Chernomodik LV, Bezrukov SM, Biophys. J 2013,104, 1933. [PubMed: 23663836]

56. Dutta D, Donaldson JG, Cell. Logistics 2012, 2, 203.

57. Giuliani M, Morbioli I, Sansone F, Chem. Commun 2015, 51, 14140.

58. Lin J, Alexander-Katz A, ACS Nano 2013, 7, 10799. [PubMed: 24251827]

59. Tatur S, Maccarini M, Barker R, Nelson A, Fragneto G, Langmuir 2013, 29, 6606. [PubMed: 23638939]

60. Adam SA, Marr RS, Gerace L, J. Cell Biol 1990, 111, 807. [PubMed: 2391365]

61. Yang W, Gelles J, Musser SM, Proc. Natl. Acad. Sci. USA 2004, 101, 12887. [PubMed: 15306682]

62. Purchased from Sigma-Aldrich (CAS: 11024-24-1). It is a mild nonionic detergent which solubilize receptors and permeabilize cytoplasm membranes.

63. Newport JW, Forbes DJ, Annu. Rev. Biochem 1987, 56, 535. [PubMed: 3304144]

64. Gall JG, J. Cell Biol 1967, 32, 391. [PubMed: 10976230]

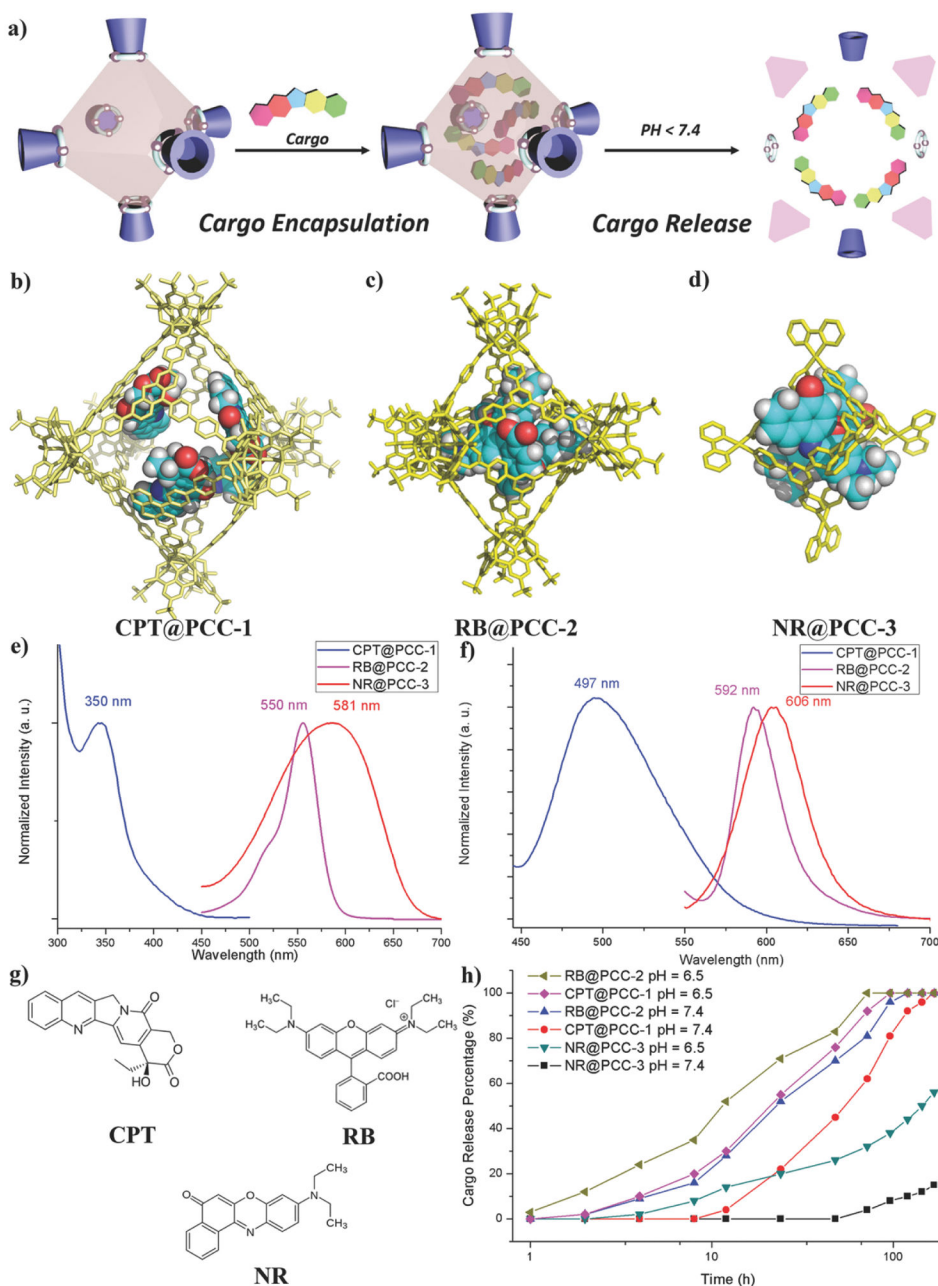65. D'Angelo MA, Hetzer MW, Trends Cell Biol. 2008, 18, 456. [PubMed: 18786826]
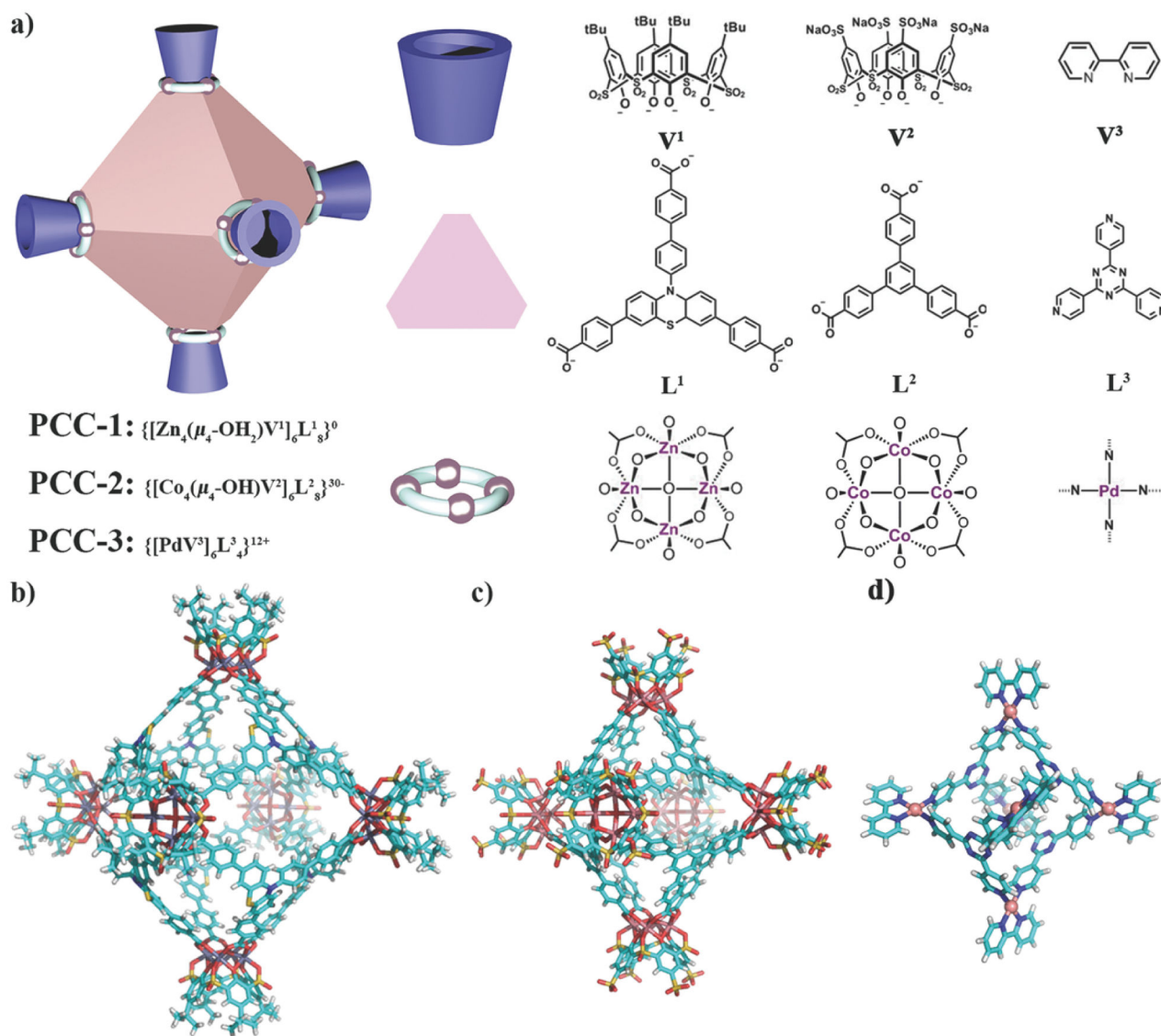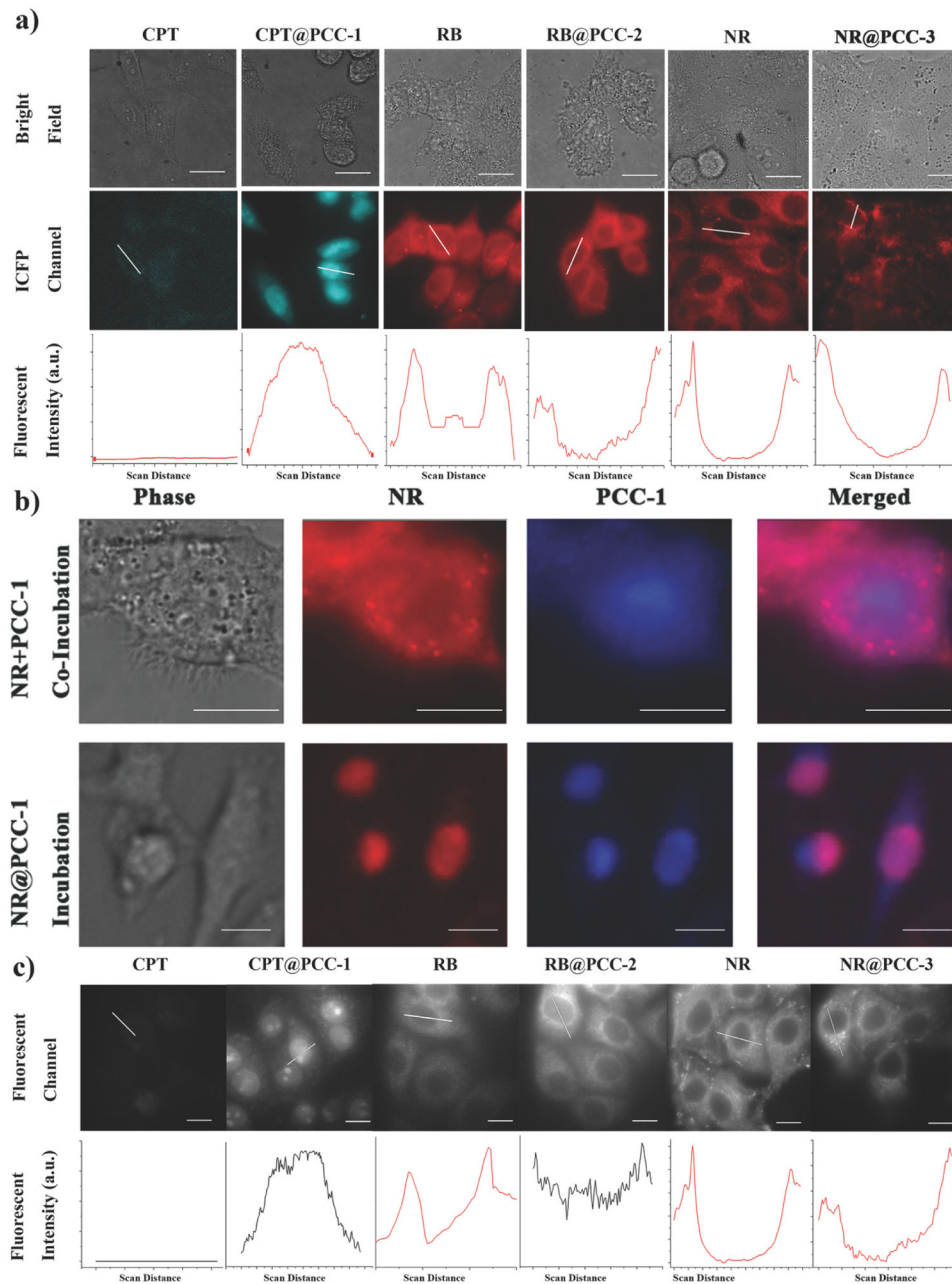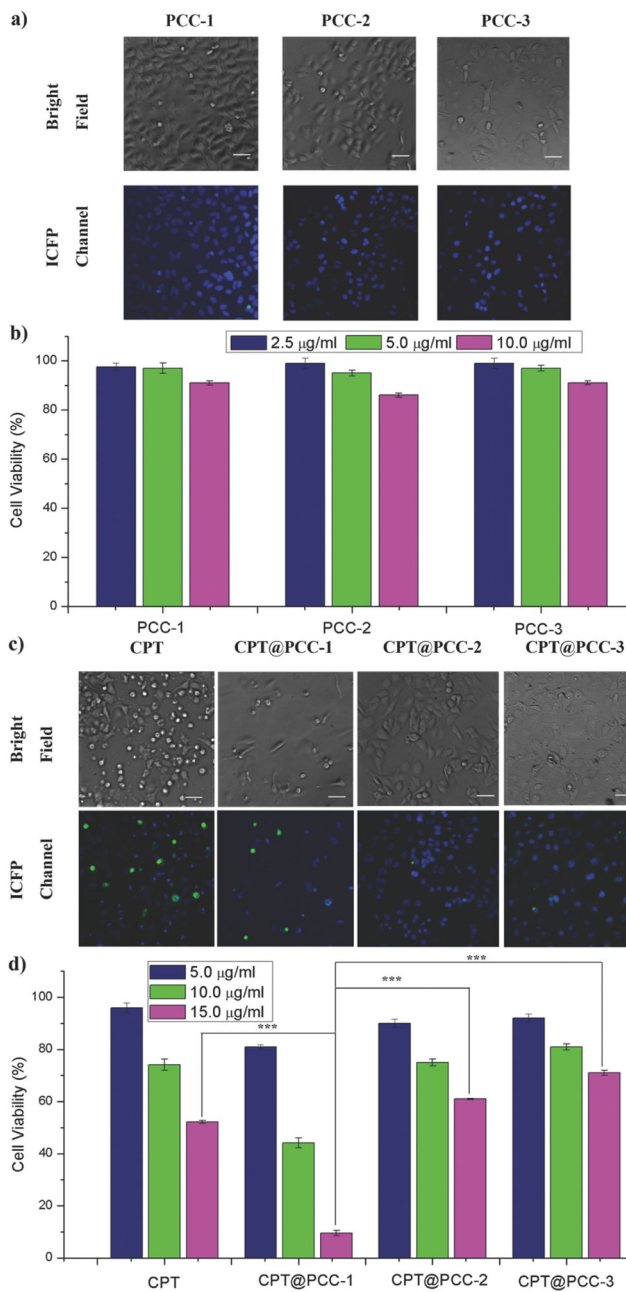
Figure 1:
Schematic structure and X-ray structure of PCCs. a) Cartoon of octahedron cage PCC and the cage components. Single-crystal X-ray crystal structure of b) PCC-1, c) PCC-2, and d) PCC-3.

Figure 2:

Cargo encapsulation and release of PCCs. a) Schematic representation of cargo encapsulation and release of PCCs. Simulated host-guest structure of b) CPT@PCC-1, c) RB@PCC-2, and d) NR@PCC-3. e) UV-vis spectrum of cargo@PCC. f) Fluorescence spectrum of cargo@PCC. g) Structure of cargo molecules. h) Accumulated cargo release of cargo@PCC according to pH = 7.4 and 6.5 in PBS solution.

Figure 3:
Intracellular transportation of cargo@PCC complexes. a) CLSM images of free cargos and cargo@PCC complexes. b) Colocalization image of HeLa cell incubated with NR@PCC-1, or co-incubated with free dye NR followed by PCC-1. c) EFM images of free cargos and cargo@PCC complexes. Scale bar: 10 μm.

Figure 4:
Cell viability of cargo@PCC complexes and control groups measured by Sytox Green assay. a) Sytox Green assay of PCC-1, PCC-2, and PCC-3 at concentration of 10 µg mL−1. b) Cell viability of PCC-1, PCC-2, and PCC-3 at concentration of 2.5, 5.0, and 10 µg mL−1. c) Sytox Green assay of CPT, CPT@PCC-1, CPT@PCC-2, and CPT@PCC-3 at concentration of 10 µg mL−1. d) Cell viability of CPT, CPT@PCC-1, CPT@PCC-2, and CPT@PCC-3 at concentration of 5.0, 10, and 15 µg mL−1. (mean ± s.d., n = 5) (***P < 0.05; Student's t-test). Green fluorescent spots indicate dead cells. Scale bar: 100 µm.

Table 1.

summary of structure, properties and celluar distribution of cargos and cargo@PCCs.

Compound	Size[a][nm]	Charge	Surface affinity[b]	Cellular distributions[c]
CPT@PCC-1	5.0	0	Lipophilic	Nucleus
NR@PCC-1	5.0	0	Lipophilic	Nucleus
CPT	0.41	0	Lipophilic	Cytoplasm
RB@PCC-2	4.2	−30	Lipophilic	Cytoplasm
RB	0.84	+1	Hydrophilic	Mitochondria
NR@PCC-3	2.8	+12	Hydrophilic	Membrane
NR	0.69	0	Lipophilic	Lipid droplet

[a] Size was measured by the single crystal size of each molecule;

[b] Surface affinity was determined according to their solubility in water or organic solvents;

[c] Cellualar distribution was determined by CLSM.